On the Correlation between Near-Field Scan Immunity and Radiated Immunity at Printed Circuit Board Level - Part I

Alexandre Boyer, Nicolas Nolhier, Fabrice Caignet, Sonia Ben Dhia

On the Correlation between Near-Field Scan Immunity and Radiated Immunity at Printed Circuit Board Level – Part I

A. Boyer, N. Nolhier, F. Caignet, S. Ben Dhia

***Abstract*—Near-Field Scan Immunity is a powerful technique to identify the root-cause of failures produced during radiated immunity tests at the integrated circuit (IC) and printed circuit board (PCB) levels. However, a prediction method of the radiated immunity level from near-field scan immunity results is still lacking. This type of method would help board designers to anticipate risks of radiated immunity non-compliance related to PCB directly after a near-field scan campaign. This two-part paper addresses this issue. In the first part, the equivalence between far-field and near-field coupling on a microstrip line is discussed in order to derive an estimator of the far-field induced voltage from near-field scan results.**

***Index Terms*— Near-field scan, radiated immunity, near-field probe, calibration**

I. Introduction

NEAR field scan immunity (NFSI) is a useful method to analyze susceptibility at the integrated circuit (IC) and printed circuit board (PCB) levels [1]. The method was described in an IEC technical specification [2]. It reveals coupling areas that can lead to failures and can assist EMC expert in identifying the root-cause of failures that may trigger during radiated immunity (RI) tests. Moreover, as shown in [3], NFSI testing requires less power than other RI tests, such as transverse electromagnetic and gigahertz transverse electromagnetic (TEM/GTEM) cells. Numerous publications have described possible applications. Examples of radio frequency (RF) injection at the IC level are presented in [4] for digital ICs, [5] for analog ICs, and [6] for RF IC, and at PCB level in [3] and [7]. NFSI is also used to analyze susceptibility to electrostatic discharge (ESD), such as in [8].

However, a specific question is not addressed in these papers: the relationship between measurement results from NFSI and those of typical RI tests with far-field (FF) illumination. Despite the limitations of the method underlined in [9], for instance local injection in NFSI is not representative of FF-illumination conditions in system-level susceptibility tests, extrapolating the RI level from the NFSI map results can warn the designer about risks of RI non-compliance, even though the impact of cables is not accounted for. Although 3D electromagnetic simulations or closed-form expressions such as in [10] can be used to compute the induced voltage on the line terminations during FF-illumination, exact knowledge of line and termination characteristics is required, which is seldom verified with practical PCB. Another practical benefit could be the definition of excitation limits for NFSI testing, based on a solid scientific basis. This question was discussed in [11] to compare direct injection with an ESD gun with a near-field (NF) probe excited by transmission line pulse (TLP). It was also recently addressed in [12] to correlate RI tests in Absorber-Lined Shielded Enclosures (ALSE) and NFSI. However, the proposed approach requires preliminary RI and NFSI tests performed on an initial PCB version. NF to FF transformation techniques, such as plane wave spectrum decomposition [13], have been used extensively for decades to extrapolate radiated emissions of antennas or PCBs from near-field scan measurements. Few comparable studies have been published for the purpose of radiated susceptibility prediction. This technique was used in [14] to improve the resolution of NFSI maps. A theoretical analysis of the correlation between NFSI maps and RI was also proposed in [15], relying on extraction of the receiving characteristics of the line under test to a given E or H-field from NFSI maps. However, this approach is valid only for linear devices and requires measurement of the phase of the induced RF voltage, which is impractical for real electronic boards.

A practical method to determine RI at the PCB level from NFSI results is still lacking. The purpose of this two-part paper is to present and validate an estimator of PCB immunity to FF illumination based on NFSI results. This estimator should provide the worst-case RI level, in order to assess radiated susceptibility risk at the end of an NFSI campaign. Due to local coupling in NF injection, only the coupling on PCB interconnects and IC is considered in this study. The proposed method aims at detecting weakness in board design (sensitive traces or ICs) regarding RI. Although cables or enclosures also have an impact on the RI of the PCB mounted in the complete system, their impact is not investigated here. Moreover, the proposed approach requires knowledge of the fields produced by the NF probe. Preliminary probe calibration is essential to determine the field produced by the NF probe at a given distance and for a given excitation. As no standard calibration

This work was supported by the Nanoscan project (CNES No. 200111/00) sponsored by the French National Centre for Space Studies (CNES).

A. Boyer, N. Nolhier, F. Caignet and S. Ben-Dhia work at the LAAS, Univ. de Toulouse, INSA, Toulouse, France (e-mail: alexandre.boyer@laas.fr, nolhier@laas.fr, fcaignet@laas.fr, sonia.bendhia@insa-toulouse.fr).

method is available for NF injection probes, this question is also addressed in this paper.

Part I of this paper focuses on the theoretical analysis of FF and NF-coupling on a common line structure in PCB, a microstrip line, in order to derive an NF-based FF coupling estimator. This estimator is then validated through simulation and measurement results. Part II will be dedicated to application of this estimator to the prediction of the RI of PCBs equipped with ICs. This paper is organized as follows: the equivalence between FF and NF couplings is discussed in Section II and the NF-based FF-coupling estimator is derived. The probe calibration process is described and validated on E and H-field probes in Section III. In the two next sections, the proposed estimator is validated through simulation and measurement results.

II. Equivalence between Far-Field Disturbance and Near-Field Injection

Let us consider a straight microstrip line terminated by passive linear loads and excited by harmonic radiated disturbances: either FF disturbance, i.e., plane wave illumination with random angles of incidence and polarization, or NF injection, i.e., an E or H-field probe placed in an arbitrary position above the line. The position of the problem is described in Fig. 1. The equivalence between these disturbances is analyzed by comparing the voltages induced at the terminal ports of the line (V_{L1} or V_{L2}).

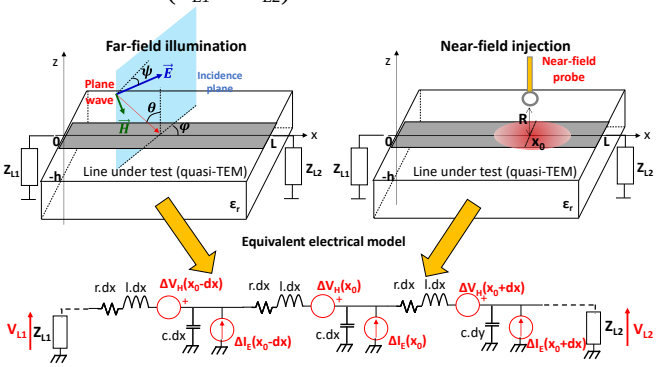

Fig. 1. Equivalent electrical model of a microstrip line exposed to an RF radiated source (plane wave or near-field source) according to the Taylor model

The interconnect is oriented along the X-axis. It is assumed to be in quasi-TEM mode and the effects of conductor and dielectric losses are disregarded. Its characteristics are assumed to be invariant, regardless of the nature of the disturbance, e.g., because of the presence of the NF probe. Whether the incoming field is uniform or not along the line, the voltage induced on line termination can be determined according to field-to-line coupling theory, which considers either only the E-field such as the Agrawal model [16], only the H-field such as the Rachidi model [17], or both the E and H-fields such as the Taylor model [18]. As local E and H-field injections are considered, the Taylor model is the most appropriate. As the line is straight and due to the line orientation, only the vertical E-field (E_Z) and tangential-H field (H_Y) couple onto the line, and induce distributed voltage and current sources ΔV_H and ΔI_E, as shown in Fig. 1. Their values are given by (1) and (2), where C_{line} is the capacitance per-unit-length of the line, $x \in [0; L]$ and $z \in [0; h]$.

$$\Delta V_H(x) = j\omega\mu_0 H_Y(x,z)dxdz \quad (1)$$

$$\Delta I_E(x) = j\omega C_{line} E_Z(x,z)dxdz \quad (2)$$

In the case of an illuminating two-conductor transmission line, according to [19], the voltages induced across both line terminals are computed by propagating and integrating the voltages produced by these distributed sources along the line, as given by (3) and (4). Γ_1 and Γ_2 are the reflection coefficients associated with termination loads, γ the complex propagation constant of the line (5), and ε_{eff} the effective permittivity of the line. For the sake of concision, only the expression of the voltage induced across load 1 will be derived, and noted V_L in the next sections.

$$V_{L1} = \int_0^L \int_{-h}^0 \frac{(1+\Gamma_1)e^{-\gamma x}}{2(1-\Gamma_1\Gamma_2 e^{-2\gamma L})}\Big(\big(1-\Gamma_2 e^{-2\gamma(L-x)}\big)\Delta V_H(x,z) + Z_C\big(1+\Gamma_2 e^{-2\gamma(L-x)}\big)\Delta I_E(x,z)\Big)\,dxdz \quad (3)$$

$$V_{L2} = \int_0^L \int_{-h}^0 \frac{(1+\Gamma_2)e^{-\gamma(L-x)}}{2(1-\Gamma_1\Gamma_2 e^{-2\gamma L})}\big((1-\Gamma_1 e^{-2\gamma x})\Delta V_H(x,z) - Z_C(1+\Gamma_1 e^{-2\gamma x})\Delta I_E(x,z)\big)dxdz \quad (4)$$

$$\gamma = j\frac{\omega}{v_P} = j\frac{\omega\sqrt{\varepsilon_{eff}}}{c_0} \quad (5)$$

The induced voltage at line terminal is related to the integration of the field along the line. Although FF disturbance illuminates the line globally, while NF injection is local, it is intuitive that, if NF and FF disturbance sources produce the same average field along the line, the induced voltage should be similar. From the similarities and differences between expressions of NF and FF-induced voltages, an estimator of the RI of the microstrip line from NF injection results will be derived.

A. Field-to-Line Coupling in the case of a Far-Field Disturbance

Let us consider a plane wave, whose incidence direction and polarization are given by the angles θ, φ and ψ, as shown in Fig. 1. They are not known and are assumed to be random and uniformly distributed on [0;π/2] for θ and [0;2π[for φ and [-π/2 ;π/2] for ψ. The presence of the air-dielectric interface and the ground plane leads to multiple reflections which affect the actual field that illuminates the line. In order to account for this effect and obtain closed-form expression of the E and H fields, the method described in [10] is reused. However, the closed-form expressions of the termination voltages proposed in [10] are not considered since they rely on the Agrawal method and the terminal loads are assumed to be matched or weakly unmatched.

The distribution of E_Z and H_Y in the substrate along the line can be extracted by separating the contributions of the transverse electric (TE) and transverse magnetic (TM) polarizations. According to the Taylor model, as only the vertical component of the E-field couples onto the line, only the TM polarization is accounted for to determine the distribution of E_Z in the substrate along the line, as given in [10] by (6), where E_0 is the amplitude of the incoming E field in free space, η_0 and γ_0 the wave impedance and the propagation constant in air, and r_{TM} the reflection coefficient at the air-dielectric

interface for TM polarization. However, both TE and TM polarizations must be considered for the distribution of H_Y in the substrate along the line. Its expression is given by (7), where H_Y^{TE} and H_Y^{TM} are the TE and TM contributions to H_Y, and r_{TE} the reflection coefficient at the air-dielectric interface for TE polarization.

$$E_Z(x,z) = \frac{E_0}{\varepsilon_r} f_E(\theta,\psi) \frac{1+r_{TM}}{1+r_{TM}e^{-\gamma_Z 2h}} \left(e^{\gamma_Z z} + e^{-\gamma_Z(z+2h)}\right) e^{-\gamma_0 x sin\theta cos\varphi} \quad (6)$$

$$H_Y(x,z) = H_Y^{TE}(x,z) sin\psi + H_Y^{TM}(x,z) cos\psi \quad (7)$$

$$H_Y^{TE}(x,z) = \frac{E_0}{\eta_0} sin\varphi \frac{1+r_{TE}}{1-r_{TE}e^{-\gamma_Z 2h}} \sqrt{\varepsilon_r - sin^2\theta} \left(e^{\gamma_Z z} + e^{-\gamma_Z(z+2h)}\right) e^{-\gamma_0 x sin\theta cos\varphi} \quad (8)$$

$$H_Y^{TM}(x,z) = \frac{E_0}{\eta_0} cos\varphi \frac{1+r_{TM}}{1+r_{TM}e^{-\gamma_Z 2h}} \left(e^{\gamma_Z z} + e^{-\gamma_Z(z+2h)}\right) e^{-\gamma_0 x sin\theta cos\varphi} \quad (9)$$

$$f_E(\theta,\psi) = sin\theta cos\psi \quad (10)$$

$$\gamma_Z = \gamma_0 \sqrt{\varepsilon_r - sin^2\theta} = j\frac{\omega}{c_0}\sqrt{\varepsilon_r - sin^2\theta} \quad (11)$$

$$r_{TE} = \frac{cos\theta - \sqrt{\varepsilon_r - sin^2\theta}}{cos\theta + \sqrt{\varepsilon_r - sin^2\theta}} \quad (12) \qquad r_{TM} = \frac{\varepsilon_r cos\theta - \sqrt{\varepsilon_r - sin^2\theta}}{\varepsilon_r cos\theta + \sqrt{\varepsilon_r - sin^2\theta}} \quad (13)$$

The expression of the voltage V_{L1}^{FF} across Z_{L1} is derived by injecting (6) and (7) in (3), which leads to (14). V_{LE}^{FF}, V_{LHTE}^{FF} and V_{LHTM}^{FF} are the contributions of E and H-field couplings, as given by (15), (16) and (17) after integration of the fields along z direction and by replacing $C_{line}.Z_c$ by $\sqrt{\varepsilon_{eff}}/c_0$ and μ_0/η_0 by $1/c_0$.

$$V_{L1}^{FF} = V_{LE}^{FF} + V_{LH}^{FF} = V_{LE}^{FF} + V_{LHTE}^{FF} + V_{LHTM}^{FF} \quad (14)$$

$$V_{LE}^{FF} = \frac{j\omega E_0}{c_0}\frac{\sqrt{\varepsilon_{eff}}}{\varepsilon_r} f_E \frac{(1+\Gamma_1)}{2(1-\Gamma_1\Gamma_2 e^{-2\gamma L})} \frac{1+r_{TM}}{1+r_{TM}e^{-\gamma_z 2h}} \frac{1-e^{-\gamma_Z 2h}}{\gamma_Z} \int_0^L e^{-\gamma_1 x}\left(1+\Gamma_2 e^{-2\gamma(L-x)}\right)dx \quad (15)$$

$$V_{LHTE}^{FF} = \frac{j\omega E_0}{c_0} sin\varphi sin\psi \frac{(1+\Gamma_1)}{2(1-\Gamma_1\Gamma_2 e^{-2\gamma L})} \frac{1+r_{TM}}{1+r_{TM}e^{-\gamma_z 2h}} \frac{1-e^{-\gamma_Z 2h}}{\gamma_Z} \int_0^L e^{-\gamma_1 x}\left(1-\Gamma_2 e^{-2\gamma(L-x)}\right)dx \quad (16)$$

$$V_{LHTM}^{FF} = \frac{j\omega E_0}{c_0} cos\varphi cos\psi \frac{(1+\Gamma_1)}{2(1-\Gamma_1\Gamma_2 e^{-2\gamma L})} \frac{1+r_{TE}}{1-r_{TE}e^{-\gamma_z 2h}} \sqrt{\varepsilon_r - sin^2\theta} \frac{1-e^{-\gamma_Z 2h}}{\gamma_Z} \int_0^L e^{-\gamma_1 x}\left(1-\Gamma_2 e^{-2\gamma(L-x)}\right)dx \quad (17)$$

$$\gamma_1 = \gamma + \gamma_0 sin\theta cos\varphi \quad (18)$$

If the substrate thickness is electrically small enough to ensure $\gamma_Z 2h \ll 1$, assumptions (19) and (20) can be made. (15), (16) and (17) can be simplified into (21) and (22), providing upper bound expressions.

$$\lim_{\omega\to 0} \frac{1+r_{TM}}{1+r_{TM}e^{-\gamma_Z 2h}} \frac{1-e^{\gamma_Z 2h}}{\gamma_Z} = 2h \quad (19)$$

$$\lim_{\omega\to 0} \frac{1+r_{TE}}{1-r_{TE}e^{-\gamma_Z 2h}} \sqrt{\varepsilon_r - sin^2\theta} \frac{1-e^{\gamma_Z 2h}}{\gamma_Z} = 2h cos\theta \quad (20)$$

$$V_{LE}^{FF} = \frac{j\omega 2hE_0}{c_0}\frac{\sqrt{\varepsilon_{eff}}}{\varepsilon_r} f_E \frac{(1+\Gamma_1)}{2(1-\Gamma_1\Gamma_2 e^{-2\gamma L})} \int_0^L e^{-\gamma_1 x}\left(1+\Gamma_2 e^{-2\gamma(L-x)}\right)dx \quad (21)$$

$$V_{LH}^{FF} = \frac{j\omega 2hE_0}{c_0} f_H \frac{(1+\Gamma_1)}{2(1-\Gamma_1\Gamma_2 e^{-2\gamma L})} \int_0^L e^{-\gamma_1 x}\left(1-\Gamma_2 e^{-2\gamma(L-x)}\right)dx \quad (22)$$

$$f_H(\theta,\psi) = cos\theta sin\varphi sin\psi + cos\varphi cos\psi \quad (23)$$

In low frequency (LF), if the line is considered electrically short, (21) and (22) can be simplified into (24) and (25). The worst-case coupling arises for $\theta = \pi/2$, $\varphi = 0$ or π and $\psi = 0$ or π, with $f_{Emax} = f_{Hmax} = 1$. The maximum amplitude of the induced voltage is given by (26). It increases linearly with frequency and proportionally to the line length.

$$V_{LE}^{FF} \approx \frac{j\omega 2hLE_0}{c_0}\frac{\sqrt{\varepsilon_{eff}}}{\varepsilon_r} f_E \frac{(1+\Gamma_1)(1+\Gamma_2)}{2(1-\Gamma_1\Gamma_2)} \quad (24)$$

$$V_{LH}^{FF} \approx \frac{j\omega 2hLE_0}{c_0} f_H \frac{(1+\Gamma_1)(1-\Gamma_2)}{2(1-\Gamma_1\Gamma_2)} \quad (25)$$

$$V_{LF\,max}^{FF} = \frac{\omega 2hLE_0}{c_0}\left|\frac{(1+\Gamma_1)}{2(1-\Gamma_1\Gamma_2)}\left(\frac{\sqrt{\varepsilon_{eff}}}{\varepsilon_r}(1+\Gamma_2)+(1-\Gamma_2)\right)\right| \quad (26)$$

In high frequency (HF), determining the worst-case coupling conditions is less straightforward, since they are related to the sum of integral terms of (21) and (22), which depends not only on the angles of arrival and polarization, but also on the substrate permittivity, frequency and Γ_2. The amplitude of the FF-induced voltage can be written according to (27), where the integral term I is given by (28). Solving this integral leads to (29), where the term k_0 compensates the linear frequency dependence of the FF-induced voltage.

$$V_{HF}^{FF} = \frac{\omega 2hE_0}{c_0}\frac{|1+\Gamma_1|}{2|1-\Gamma_1\Gamma_2 e^{-2\gamma L}|} I \quad (27)$$

$$I = \left|\int_0^L e^{-\gamma_1 x}\left(\frac{\sqrt{\varepsilon_{eff}}}{\varepsilon_r} f_E\left(1-\Gamma_2 e^{-2\gamma(L-x)}\right) + f_H\left(1-\Gamma_2 e^{-2\gamma(L-x)}\right)\right)dx\right| \quad (28)$$

$$I = \left|\frac{\frac{\sqrt{\varepsilon_{eff}}}{\varepsilon_r} f_{E+} f_H}{\gamma_a}(1-e^{-\gamma_a L}) + \frac{\frac{\sqrt{\varepsilon_{eff}}}{\varepsilon_r} f_{E-} f_H}{\gamma_b}(1-e^{-\gamma_b L})\Gamma_2 e^{-2\gamma L}\right| \quad (29)$$

$$\gamma_{a,b} = \gamma_0\left(sin\theta cos\varphi \pm \sqrt{\varepsilon_{eff}}\right) \quad (30)$$

The exact extreme value of integral term (29) cannot easily be found, but the upper bound given by (31) can be extracted, which depends on θ, φ and ψ. From Monte-Carlo simulation with various angles of arrival, polarization, loading conditions and frequencies, the upper bound given by (32) can be found, for $\frac{\sqrt{\varepsilon_{eff}}}{\varepsilon_r} \le \frac{1}{\sqrt{\varepsilon_{eff}}}$, and can be simplified in (33). Injecting this upper bound in (27) provides the expression of the worst-case FF-induced voltage on line terminal, given in (34).

$$I \le \frac{2}{|\gamma_0|}\left|\frac{\frac{\sqrt{\varepsilon_{eff}}}{\varepsilon_r} f_{E+} f_H}{sin\theta cos\varphi + \sqrt{\varepsilon_{eff}}} + \frac{\frac{\sqrt{\varepsilon_{eff}}}{\varepsilon_r} f_{E-} f_H}{sin\theta cos\varphi - \sqrt{\varepsilon_{eff}}}\Gamma_2\right| \quad (31)$$

$$I \le \frac{2}{|\gamma_0|}\left(\frac{1-\frac{\sqrt{\varepsilon_{eff}}}{\varepsilon_r}}{\sqrt{\varepsilon_{eff}}-1} + \frac{1+\frac{\sqrt{\varepsilon_{eff}}}{\varepsilon_r}}{\sqrt{\varepsilon_{eff}}+1}|\Gamma_2|\right) \quad (32)$$

$$I \le \frac{2}{|\gamma_0|}\frac{1-\frac{\sqrt{\varepsilon_{eff}}}{\varepsilon_r}}{\sqrt{\varepsilon_{eff}}-1}(1+|\Gamma_2|) \quad (33)$$

$$V_{HF\,max}^{FF} = 4hE_0\frac{|1+\Gamma_1|}{2|1-\Gamma_1\Gamma_2 e^{-2\gamma L}|}\frac{1-\frac{\sqrt{\varepsilon_{eff}}}{\varepsilon_r}}{\sqrt{\varepsilon_{eff}}-1}(1+|\Gamma_2|) \quad (34)$$

In order to validate the upper bound expressions of the worst-case induced voltage on an illuminated microstrip line, simulations made with the 3D electromagnetic solver FEKO [20] are performed. Two validation cases are considered. The first line (Line 1) is designed on a 0.4 mm thick substrate with ε_r equal to 2.2. Its width is set to 0.5 mm to match the line to 82 **Ω**. The second line (Line 2) is designed on a 1.6 mm thick substrate with ε_r equal to 4.5. Its width is set to 3 mm to match the line to 50 **Ω**. Both lines are 50 mm long and are terminated

by 80 Ω resistors. The worst-case coupling is simulated between 100 MHz and 10 GHz by repeating simulations, sweeping θ, φ and ψ on their definition range with a step of 10°, and extracting the maximum induced voltage. The simulation results are plotted in Fig. 2 and compared with the asymptotic upper bound of the worst-case FF coupling, given by the minimum value of (26) and (34). Excellent agreement between the simulated worst-case induced voltage and the LF upper-bound is obtained. When the line becomes electrically long, (34) provides an upper limit of the worst-case coupling. It should be underlined that this upper limit can exceed the actual extreme value of the induced voltage. Depending on line characteristics, terminations and frequency, the maximum value of integral I can be lower than the limit provided by (33). Nevertheless, the overestimation of the worst-case coupling remains in an acceptable range. Around 1 GHz, both lines start to be electrically long, showing an intermediary frequency range where both asymptotic limits (26) and (34) tend to overestimate the worst-case induced voltage. The transition between LF and HF upper bounds can be smoothed, as described in Section II.C.

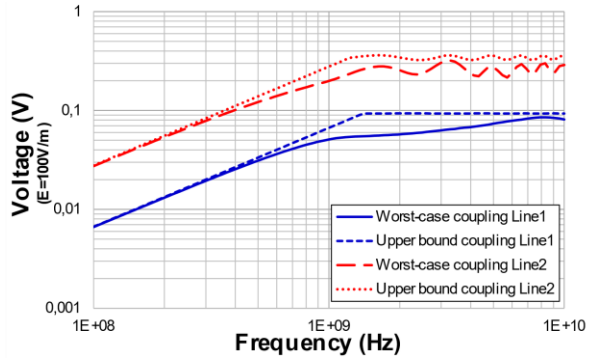

Fig. 2. Comparison between simulation of the worst-case voltage induced on two microstrip lines by a 100 V/m far-field illumination and the asymptotic upper bounds (26) and (34)

B. Field-to-Line Coupling in the case of a Near-Field Disturbance

Let us suppose now that the disturbance is produced by an NF probe placed in close proximity above the victim line (in practice a few millimeters above the PCB surface), as described in Fig. 1. The probe is placed an arbitrary position $x_0 \in [-L/2;L/2]$. During the NFSI test, the position can be swept over all the line. Depending on the nature of the probe, they produce either a local intense E or H-field. In the following parts, the stray field components will be disregarded. Contrary to the FF illumination case, the amplitude of the field produced by the injection probe along the line is not uniform, and tends to decrease rapidly with the distance. In Section III, extraction of the E and H field distribution in the vicinity of the probe will be addressed. In this part, these distributions, E_Z^{NF} and H_Y^{NF}, respectively are assumed to be perfectly known. From (1), (2) and (3), by replacing $C_{line}.Z_c$ by $\sqrt{\varepsilon_{eff}}/c_0$, the expressions of the induced voltages due to E and H-field injections are given by (35) and (36).

$$V_{LE}^{NF} = \frac{j\omega\sqrt{\varepsilon_{eff}}}{c_0}\frac{(1+\Gamma_1)}{2(1-\Gamma_1\Gamma_2 e^{-2\gamma L})}\int_0^L\int_{-h}^0 e^{-\gamma x}\left((1+\Gamma_2 e^{-2\gamma(L-x)})E_Z^{NF}(x,z)\right)dxdz \quad (35)$$

$$V_{LH}^{NF} = j\omega\mu_0\frac{(1+\Gamma_1)}{2(1-\Gamma_1\Gamma_2 e^{-2\gamma L})}\int_0^L\int_{-h}^0 e^{-\gamma x}\left((1-\Gamma_2 e^{-2\gamma(L-x)})H_Y^{NF}(x,z)\right)dxdz \quad (36)$$

In order to obtain a form similar to those in FF illumination, two simplifications are made. The first one consists in assuming that the NF coupling is extremely local, i.e., most of the coupling arises on an electrically short section centered around x_0. The complex exponential terms in (35) and (36) can be moved outside the integral. The second simplification consists in replacing the integral of the E or H field along z direction by the field obtained at an average height z_0 (comprised between -h and 0), where the field produced by the probe is equal to the average field between the line and the ground plane. With these simplifications, (35) and (36) are rewritten in (37) and (38).

$$V_{LE}^{NF} = \frac{j\omega h\sqrt{\varepsilon_{eff}}}{c_0}\frac{(1+\Gamma_1)}{2(1-\Gamma_1\Gamma_2 e^{-2\gamma L})}e^{-\gamma x_0}\left(1+\Gamma_2 e^{-2\gamma(L-x_0)}\right)\frac{L}{L}\int_0^L E_Z^{NF}(x-x_0,z_0)dx \quad (37)$$

$$V_{LH}^{NF} = j\omega\mu_0 h\frac{(1+\Gamma_1)}{2(1-\Gamma_1\Gamma_2 e^{-2\gamma L})}e^{-kx_0}\left(1-\Gamma_2 e^{-2\gamma(L-x_0)}\right)\frac{L}{L}\int_0^L H_Y^{NF}(x-x_0,z_0)dx \quad (38)$$

The ratio L/L appears in (37) and (38) to introduce the average fields $\overline{E_Z^{NF}(x_0)}$ and $\overline{H_Y^{NF}(x_0)}$ produced by the injection probe along the line, when the probe is located at $x = x_0$, whose expressions are given by (39) and (40). Finally, the integrals of the field along the line are replaced by the average fields and the expressions (41) and (42) are derived.

$$\overline{E_Z^{NF}(x_0)} = \frac{1}{L}\int_0^L E_Z^{NF}(x-x_0,z_0)dx \quad (39)$$

$$\overline{H_Y^{NF}(x_0)} = \frac{1}{L}\int_0^L H_Y^{NF}(x-x_0,z_0)dx \quad (40)$$

$$V_{LE}^{NF} = \frac{j\omega hL\sqrt{\varepsilon_{eff}}}{c_0}\frac{(1+\Gamma_1)e^{-\gamma x_0}}{2(1-\Gamma_1\Gamma_2 e^{-2\gamma L})}\left(1+\Gamma_2 e^{-2\gamma(L-x_0)}\right)\overline{E_Z^{NF}(x_0)} \quad (41)$$

$$V_{LH}^{NF} = j\omega\mu_0 hL\frac{(1+\Gamma_1)e^{-\gamma x_0}}{2(1-\Gamma_1\Gamma_2 e^{-2\gamma L})}\left(1-\Gamma_2 e^{-2\gamma(L-x_0)}\right)\overline{H_Y^{NF}(x_0)} \quad (42)$$

In LF, if the microstrip line can be considered to be electrically short, (41) and (42) are simplified in (43) and (44). When the induced voltages are expressed according to the average field produced by the injection probe over the line, they are proportional to the frequency and line length.

$$V_{LE\,LF}^{NF} = \frac{\omega hL\sqrt{\varepsilon_{eff}}}{c_0}\left|\frac{(1+\Gamma_1)(1+\Gamma_2)}{2(1-\Gamma_1\Gamma_2)}\right|\overline{E_Z^{NF}(x_0)} \quad (43)$$

$$V_{LH\,LF}^{NF} = \omega hL\mu_0\left|\frac{(1+\Gamma_1)(1-\Gamma_2)}{2(1-\Gamma_1\Gamma_2)}\right|\overline{H_Y^{NF}(x_0)} \quad (44)$$

In HF, the exponential terms cannot be disregarded. Depending on the frequency and probe position, the terms $1 \pm \Gamma_2 e^{-2\gamma(L-x_0)}$ present periodical-spaced minima and maxima. It should be noted that these positions do not coincide in E and H-field injection. Thus, scanning in only one arbitrary position x_0 is not sufficient to completely characterize the RI of a device under test (DUT), since the NF-induced voltage profiles will present a series of minima and maxima over the frequency, contrary to the FF-induced voltage. The dependency to the probe position can be removed if the maximal NF-induced is determined. The advantage of the near-field scan is that the probe position is changed during the test so the worst-case coupling positions, x_{Emax} and x_{Hmax}, and the related maximum

NF-induced voltage can be found at each frequency. If a scan is performed with a sufficiently small scanning step, positions x_{Emax} and x_{Hmax} can be found precisely. The amplitudes of the maximum NF-induced voltages are given by (45) and (46), where $\overline{E_{Z\,max}^{NF}}$ and $\overline{H_{Y\,max}^{NF}}$, given by (47) and (48) are the average fields produced by the injection probe along the line when it is placed in worst-case coupling positions, determined during the near-field scan test.

$$V_{LE\,max}^{NF} = \frac{\omega h L \sqrt{\varepsilon_{eff}}}{c_0} \left| \frac{(1+\Gamma_1)(1+|\Gamma_2|)}{2(1-\Gamma_1\Gamma_2 e^{-2\gamma L})} \right| \left| \overline{E_{Z\,max}^{NF}} \right| \quad (45)$$

$$V_{LH\,max}^{NF} = \omega h L \mu_0 \left| \frac{(1+\Gamma_1)(1+|\Gamma_2|)}{2(1-\Gamma_1\Gamma_2 e^{-2\gamma L})} \right| \left| \overline{H_{Y\,max}^{NF}} \right| \quad (46)$$

$$\overline{E_{Z\,max}^{NF}} = \overline{E_Z^{NF}(x_{Emax})} \quad (47)$$

$$\overline{H_{Y\,max}^{NF}} = \overline{H_Y^{NF}(x_{Hmax})} \quad (48)$$

In order to validate the upper bound expressions of the worst-case induced voltage by a local E or H-field injection on a microstrip line, simulations made with the 3D electromagnetic solver FEKO [20] are performed. Case study Line 1 described in Section II.B is reused. The line is terminated by a 20 Ω resistor on one end and by 200 Ω on the other end. The E NF probe is modeled by an elementary electric dipole with a moment of 1 µA·m placed at 1 mm above the line. The H NF probe is modeled by an elementary magnetic dipole with a moment of 1 µA·m² placed at 1 mm above the line. Simulations are repeated for different positions of the injection probes, which are moved between both line ends with a step of 2.5 mm. At each frequency, simulation results are processed to extract the worst-case coupling positions x_{Emax} and x_{Hmax}, and the maximum induced voltages $V_{LE\,max}^{NF}$ and $V_{LH\,max}^{NF}$ are kept. The simulation results are plotted in Fig. 3 and compared with the LF and HF upper bounds of the worst-case NF coupling, given by (43) and (45) for E-field injection, and (44) and (46) for H-field injection. The simulations of the worst-case induced voltages are in good agreement with the calculated LF upper bounds up to several hundred MHz, as long as the line is electrically small. Above 1.1 GHz, the line length is larger than one quarter of the wavelength and can be considered electrically long. The simulated worst-case induced voltages fit with the calculated HF upper bounds.

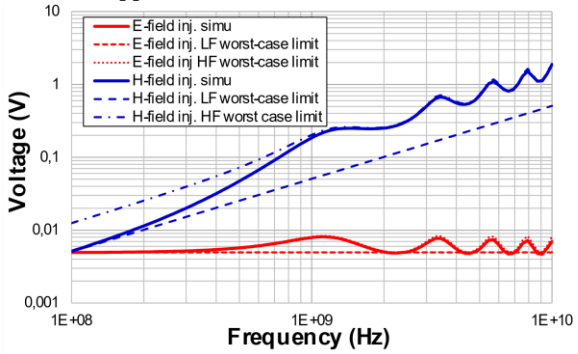

Fig. 3. Comparison between the simulation of the worst-case voltage induced on a microstrip line during E and H-field injection and the calculated LF and HF upper bounds

C. Relationship between Far-Field and Near-Field induced Voltage

The comparison between the different expressions of FF and NF-induced voltage on a microstrip line shows differences so that the exact evaluation of the FF coupling in a particular illumination condition from NFSI results is not possible. The main differences are related to the lack of the angles of arrival and polarization in the NF coupling expressions, and injection position in FF coupling expressions. Moreover, FF coupling is distributed while NF coupling is local, so the effects due to line propagation are not exactly the same in FF and NF coupling expressions. Finally, in FF coupling, both E and H-field coupling are superimposed, while in NF coupling either E or H-field is mainly coupled. In practice, except if the phase is measured, it is not possible to determine how E and H-field coupling contributions measured in NFSI tests should be added, to estimate exactly how they are actually combined during FF illumination.

However, the expressions of the upper bounds of the induced voltages exhibit many similarities, especially the influence of the terminal loads and line propagation. They are sufficient to use NFSI results as an upper bound of the worst-case FF coupling, regardless of the loading conditions, line geometry and materials. To compare FF and NF couplings, a first step consists in scaling NF-induced voltages in order to determine what would be the induced voltage if the average E or H-field produced by the injection probe were identical to the plane wave excitation. The scaling consists in multiplying (43) by $2E_0/\left|\overline{E_{Z\,max}^{NF}}\right|$ and (44) by $2E_0/\left(\eta_0\left|\overline{H_{Y\,max}^{NF}}\right|\right)$. First, let us consider the LF assumption. The comparison of the worst-case FF-induced voltage (21) with the maximum voltages induced during E and H-field injection ((36) and (37)) shows that (26) can be upper bounded by the sum of the scaled versions of (36) and (37), if the E-field related term is divided by ε_r. This LF FF coupling estimator from NFSI results is given by (49). Importantly, this estimator may overestimate the worst-case FF coupling when the relative phase of $V_{LE\,LF}^{NF}$ and $V_{LH\,LF}^{NF}$ is not accessible.

$$V_{L1\,LF}^{NF\to FF} = \frac{2E_0}{\left|E_{Z\,max}^{NF}\right|\varepsilon_r} V_{LE\,LF}^{NF} + \frac{2E_0}{\eta_0\left|H_{Y\,max}^{NF}\right|} V_{LH\,LF}^{NF} \geq V_{LF\,max}^{FF} \quad (49)$$

In HF, the worst-case FF-induced voltage (34) can also be upper bounded by a sum of the maximum voltages induced during E and H-field injection ((45) and (46)). However, this estimator tends to overestimate (34) since it does not depend on line length and frequency, contrary to (45) and (46). A simple change can be made to the previous estimator, consisting in multiplying (45) and (46) by $c_0/(\omega L)$ and a corrective term dependent on ε_r and ε_{eff} to obtain an estimator equal to the worst-case FF-induced voltage $V_{HF\,max}^{FF}$ (34). The HF FF coupling estimator from NFSI results is given by (50). Interestingly, the worst-case E and H-NF couplings are identical. The practical importance is that only E or H-field injection could be necessary to estimate the RI level in FF illumination. One practical issue with this estimator is that it requires the knowledge of ε_{eff} or v_P. Although they can be extracted from S

parameter measurement, typical PCB lines are not usually terminated by RF ports, meaning that this type of extraction cannot be made precisely. A simple solution consists in considering that ε_{eff} is equal to ε_r, whose value is known in practice. A simplified version of the HF estimator is given by (51).

$$V_{L1\,HF}^{NF\to FF} = \frac{2E_0c_0}{\omega L}\frac{1-\frac{\sqrt{\varepsilon_{eff}}}{\varepsilon_r}}{\sqrt{\varepsilon_{eff}}-1}\left(\frac{V_{LE\,max}^{NF}}{\left|E_{Z\,max}^{NF}\right|\sqrt{\varepsilon_{eff}}}+\frac{V_{LH\,max}^{NF}}{\eta_0\left|H_{Y\,max}^{NF}\right|}\right) \quad (50)$$

$$V_{L1\,HF}^{NF\to FF} = \frac{2E_0c_0}{\omega L\sqrt{\varepsilon_r}}\left(\frac{V_{LE\,max}^{NF}}{\left|E_{Z\,max}^{NF}\right|\sqrt{\varepsilon_{eff}}}+\frac{V_{LH\,max}^{NF}}{\eta_0\left|H_{Y\,max}^{NF}\right|}\right) \quad (51)$$

Another issue is related to the frequency limit between both estimators and the definition of a unique estimator. A convenient method to smooth the transition between LF and HF estimators consists in multiplying (52) by a first-order high pass filter with a cut-off frequency of f_C as given by (53).

$$V_{L1}^{NF\to FF} = \frac{2E_0.V_{LE\,max}^{NF}}{\overline{E_{Z\,max}^{NF}}\varepsilon_r\sqrt{1+\left(\frac{f}{f_C}\frac{\varepsilon_r}{\sqrt{\varepsilon_{eff}}}\right)^2}}+\frac{2E_0.V_{LH\,max}^{NF}}{\eta_0\overline{H_{Y\,max}^{NF}}\sqrt{1+\left(\frac{f}{f_C}\right)^2}} \quad (52)$$

$$f_C = \frac{c_0}{2\pi L}\frac{\sqrt{\varepsilon_{eff}}-1}{1-\frac{\sqrt{\varepsilon_{eff}}}{\varepsilon_r}} \quad (53)$$

III. Near-Field Injection Probe Calibration

As shown in the previous section, the estimation of the worst-case FF-induced voltage from NFSI results relies on knowledge of the NF distribution produced by injection probes along the line under test. Therefore, preliminary calibration is needed to characterize the field produced by the probe. Unfortunately, contrary to an NF probe used for emission purposes, no standard calibration process is currently available to extract a reduced set of parameters to determine the field distribution produced by the probe, regardless of the nearby environment.

Several options to calibrate an NF injection probe can be found in the literature. One approach presented in [21] proposes to use a matched microstrip line as a reference coupling structure, in order to determine the coupling with an H-field probe, which is expressed as a mutual coupling coefficient. Although electrical simulators handle this coefficient, it depends on probe position and must be determined for a large number of positions. It also depends on the line characteristics so the coefficient is valid only for the reference line. In [3], the same calibration line is used but to determine the required probe excitation to induce a reference voltage (e.g., 1 V) on the calibration line. The main advantage of this approach is practical, as it may provide a raw order of the induced voltage on a disturbed PCB. However, it does not solve the previous problem and cannot provide the field distribution produced by the probe. A convenient alternative to determine field distribution consists in assuming that injection probes, due to their small size, are equivalent to elementary dipoles. In [22], TEM cell measurements are proposed to extract the equivalent electric or magnetic moment of the probe. However, this calibration procedure is not sufficient to verify that the field distribution of the probe complies with the one created by a dipole. Moreover, the actual position of the center of the equivalent dipole cannot be extracted with this method. In this section, a calibration method of an injection probe is proposed to extract a reduced set of parameters to determine their field distribution in the NF region. It reuses the approach described initially in [23] and the equivalent dipole assumption.

A. Description of the Calibration Process

The general test set-up to calibrate the injection NF probe is described in Fig. 4. The probe is placed precisely by a near-field scanner at a controlled position (x_P,y_P) and a scan altitude R above the center of a properly calibrated receiving NF probe. It is characterized by two parameters: its performance factor (PF), which relates the voltage measured at the probe terminal and the incoming field, and its effective height h_{eff}, which is the distance between the probe tip and the actual measurement point of the field, called the center in Fig. 4. R is the separation distance between probe tips. Calibration consists in verifying and extracting an elementary electric or magnetic dipole model, from the measurement of field distribution around the injection probe. The expressions of the fields produced by vertically oriented electric and magnetic dipoles, oriented according to Fig. 5, are given by (54) to (57), where β_0 is the phase constant in vacuum, which can be simplified according to the $1/r^3$ law for short separation distance.

The probe separation distance R and the distance r between the measurement point and the dipole center must be distinguished, since the reception probe does not measure the field exactly at its tip and the injection probe is equivalent to a dipole not centered on the probe tip. The relationship between R and r is given by (58), where the injection height h_{inj} is the distance between the probe extremity and the center of the equivalent dipole. The validity of this model can be verified experimentally if the field produced by the injection probe decays inversely to the cube of the distance r between the actual center of the receiving probe and the dipole center. The injection probe model contains two parameters to be extracted: the dipole moment (m_E or m_H), for each frequency and for a reference excitation (e.g., 1 W), and the injection height.

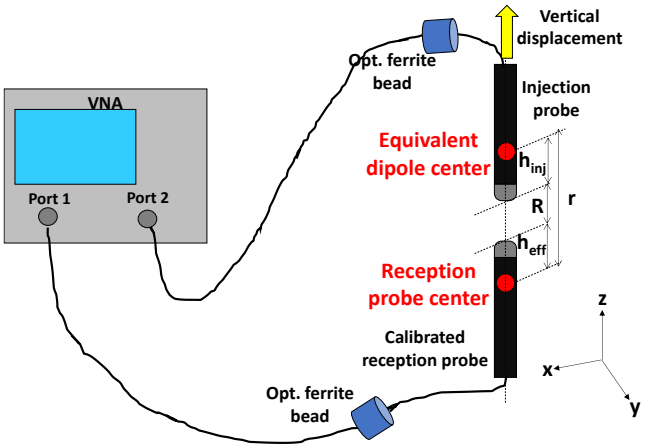

Fig. 4. Calibration set-up of injection near-field probe

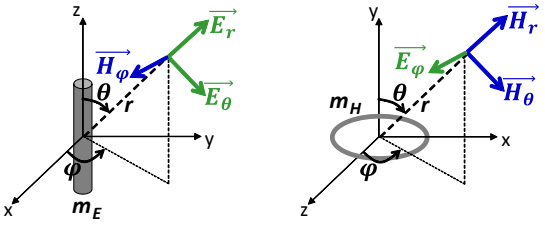

Fig. 5. Orientation of electric and magnetic dipoles

$$E_r = \frac{\eta_0\beta_0^2}{2\pi} m_E cos\theta \left(\frac{1}{\beta_0^2 r^2} - \frac{j}{\beta_0^3 r^3}\right) e^{-j\beta_0 r} \approx \frac{-jm_E}{2\pi r^3}\frac{cos\theta}{\omega\varepsilon_0} \quad (54)$$

$$E_\theta = \frac{\eta_0\beta_0^2}{4\pi} m_E sin\theta \left(\frac{j1}{\beta_0 r} + \frac{1}{\beta_0^2 r^2} - \frac{j}{\beta_0^3 r^3}\right) e^{-j\beta_0 r} \approx \frac{-jm_E}{4\pi r^3}\frac{sin\theta}{\omega\varepsilon_0} \quad (55)$$

$$H_r = \frac{j\omega\mu_0\beta_0^2}{2\pi\eta_0} m_H cos\theta \left(\frac{1}{\beta_0^2 r^2} - \frac{j}{\beta_0^3 r^3}\right) e^{-j\beta_0 r} \approx \frac{m_H cos\theta}{2\pi r^3} \quad (56)$$

$$H_\theta = \frac{j\omega\mu_0\beta_0^2}{4\pi\eta_0} m_H sin\theta \left(\frac{j}{\beta_0 r} + \frac{1}{\beta_0^2 r^2} - \frac{j}{\beta_0^3 r^3}\right) e^{-j\beta_0 r} \approx \frac{m_H sin\theta}{4\pi r^3} \quad (57)$$

$$r = R + h_{eff} + h_{inj} \quad (58)$$

The field distribution produced by the injection probe is determined from the measurement of the transmission coefficient S_{12} between the injection and receiving probes, e.g., using a vector network analyzer (VNA). From the measured S_{12}, the E or H-field produced by the injection probe excited by a reference forward voltage V_{forw} or power P_{forw} are given by (59) or (60), where PF_E and PF_H refer to the PF of the reception E and H-field probes. E-field probe calibration can be affected by common-mode resonances due to field coupling on the outer shielding of the probe. To attenuate them, ferrite beads can be added around the cables connecting the probes to the VNA.

$$E(x_0, y_0, r, \omega) = \frac{S_{12}(x_0,y_0,r,\omega)}{PF_E(\omega)} V_{forw} = \frac{S_{12}(x_0,y_0,r\omega)}{PF_E(\omega)} \sqrt{Z_C P_{forw}} \quad (59)$$

$$H(x_0, y_0, r, \omega) = \frac{S_{12}(x_0,y_0,r,\omega)}{PF_H(\omega)} V_{forw} = \frac{S_{12}(x_0,y_0,r\omega)}{PF_H(\omega)} \sqrt{Z_C P_{forw}} \quad (60)$$

The measurement is done at several separation distances R between both probes. The first step consists in verifying the assumption of an elementary electric or magnetic dipole and extracting h_{inj}. The evolution of the E or H field is plotted vs. the distance r, when both probes are face to face. Then, h_{inj} is adjusted to ensure that the field decays with r according to an inverse cubic relationship. If this type of relationship is verified for a given value of h_{inj}, the dipole assumption is validated and the equivalent moment is extracted.

B. Calibration Results

The calibration procedure is tested on two hand-made injection probes. The first one is a normal E-field probe which consists of a 4 mm long tip at the end of a semi-rigid coaxial cable. The second one is a tangential H-field probe made of a 5 mm diameter circular loop that terminates a semi-rigid coaxial cable. The E and H-field distribution produced by these injection probes are characterized by two receiving probes: XFE04s E-field probe and RFR0.3-3 H-field probe, designed by Langer EMV. Both probes are given from 30 MHz to 3 GHz. They have been carefully calibrated up to 3 GHz according to the method described in [24]. Calibration of both probes is done at several scanning heights above several structures under test to ensure that PF is not affected by probe position and calibration structure. Their h_{eff} are equal to 2 and 0.9 mm, respectively.

S_{12} measurements are performed between injection and receiving probes, with R ranging from 0.5 to 8 mm. The evolution of the normalized S_{12} according to the distance $R+h_{eff}$ is plotted in the left parts of Figs 6 and 7. S_{12} decreases with the distance, but not as rapidly as an inverse cube law. For each injection probe, h_{inj} is adjusted in order to ensure that S_{12} decays according to the inverse cube of r: h_{inj} is set to 2.3 mm for the H-field probe (nearly the radius of the probe) and 3.2 mm for the E-field probe. The results are plotted on the right parts of Figs. 6 and 7, showing that the field decays with the distance in accordance with the elementary dipole model.

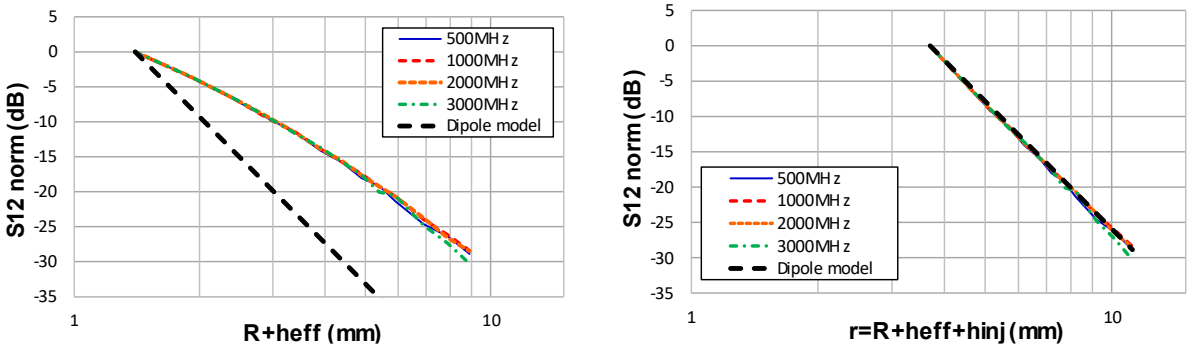

Fig. 6. Extraction of the injection height of the H-field injection probe: normalized S12 vs. $R+h_{eff}$ (left), adjustment of h_{inj} (right)

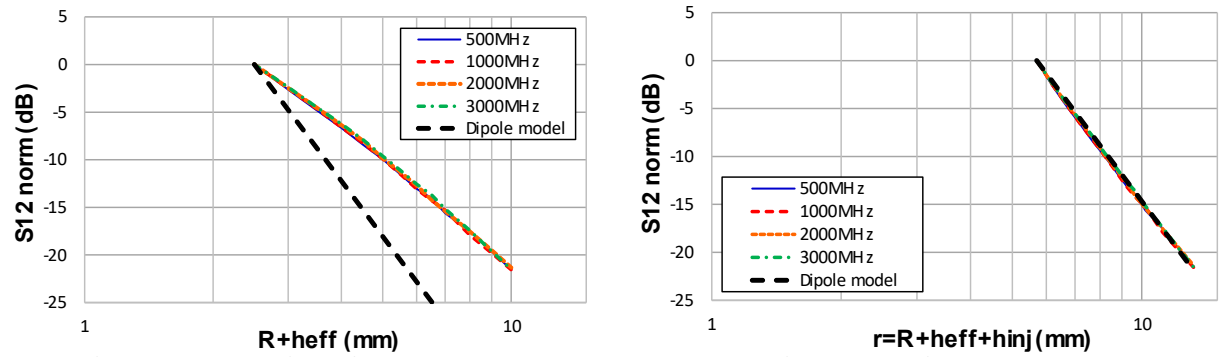

Fig. 7. Extraction of the injection height of the E-field injection probe: normalized S12 vs. $R+h_{eff}$ (left), adjustment of h_{inj} (right)

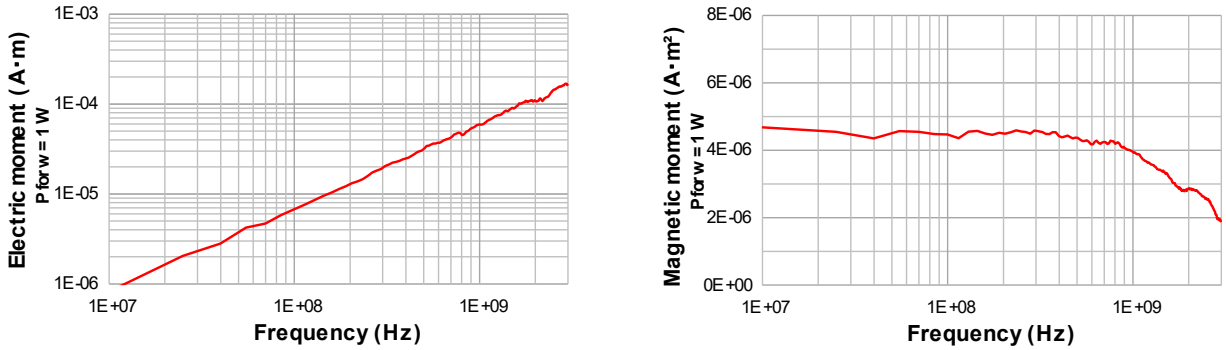

Fig. 8. Extracted electric moment of the E-field injection probe (left) – magnetic moment of the H-field injection probe (right)

Finally, the moments of both probes are extracted from S_{12} measurement according to (54) and (57), as shown in Fig. 8 for an excitation power of 1 W. The results show that the moment of the H-field probe is nearly constant up to 1 GHz and then tends to decrease with frequency due to the parasitic inductance of the probe. The moment of the E-field probe increases linearly with frequency at least up to 3 GHz.

C. Influence of Substrate on the field produced by the Injection Probe

Equations (54) to (57) are valid only if the dipole is placed in free space. However, in practical NFSI at the PCB level, probes are placed at less than a few millimeters above the board surface, whose dielectric material and metal layers may severely affect the field distribution. For H-field injection, only the presence of metal layers modifies the H-field distribution. In the case of a microstrip line, the effect of the ground plane can be conveniently accounted for by the image theory. A second virtual magnetic dipole is placed under the ground plane anti-symmetrically to the actual dipole.

The influence of the grounded substrate makes the computation of the E-field produced by the E-field probe more complex. The air-dielectric interface and the ground plane lead to multiple reflections between these interfaces. In order to determine a closed-form expression of the E-field in such a non-homogeneous medium, if losses remain reasonable enough to be considered negligible, the multiple image method is a convenient extension of the classical image theory. The effect of the ground plane and the air-dielectric interface can be modeled by a series of multiple virtual and partial images whose distance to the substrate surface and excitation depend on substrate thickness h, dipole altitude R, and dielectric permittivity ε_r. The method, initially presented in [25], was used to derive characteristic impedance and propagation velocity of a microstrip line. It is reused here to determine closed-form expressions of the near E-field produced by an injection probe modeled as an elementary electric dipole above a two-layer lossless substrate.

Let us consider a vertical electric dipole m_E placed at a distance R above the substrate surface and a measurement point P within the substrate. The E-field is the sum of the direct contribution of this dipole and those due to the multiple reflections, modeled as virtual dipoles placed under the substrate surface, as illustrated in Fig. 9. The primary image m_1 is related to the transmission through the air-dielectric interface followed by a reflection on the ground plane, respectively. The other secondary images, $m_{2A}^{\pm n}$ and $m_{2B}^{\pm n}$, are related to the multiple reflections between both interfaces of the direct contribution and the primary image, respectively. The contribution of the moment m_E to the E-field in P is given by a function $E(m,r)$ (given by (54) or (55)). The contribution of all the partial images to the E-field can be determined by (60), where the first term is the direct contribution of m_E, the second term is due to the reflection to the ground plane, and the two last infinite sums are the contributions of the secondary images. For a microstrip line designed on a typical PCB for electronic products (h ranging between 0.2 and 2 mm, w < 3 mm, L < 10 cm, ε_r between 2 and 5) and for scan measurement height less than 10 mm, 5 to 8 secondary images are sufficient to converge at less than 1 % of the actual E-field value. In this study, a number of 20 secondary images is selected to solve (61).

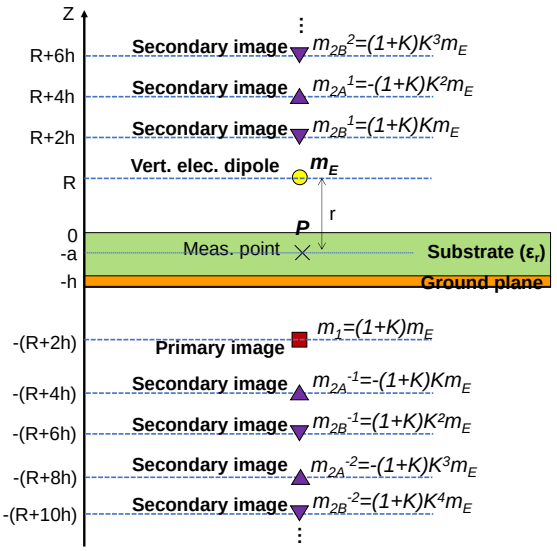

Fig. 9. Multiple partial image model for an elementary vertical electric dipole placed above a grounded substrate

$$E = E(K'm_E, r) + E(K'm_E, r + 2(h-a)) - \sum_{n=1}^{\infty}\left[E\left(K'^{K^{2n}m_E}, r + 4nh\right) + E\left(K'^{K^{2n-1}m_E}, r - 2a + 4nh\right)\right] + \sum_{n=1}^{\infty}[E(K'K^{2n-1}m_E, r + (4n-2)h) + E(K'K^{2n}m_E, r - 2a + (4n+2)h)] \quad (60)$$

$$K = \frac{1-\varepsilon_r}{1+\varepsilon_r} \quad (61)$$

$$K' = 1 + K \quad (62)$$

D. Validation of the Injection Probe Calibration

In order to validate the computation of the field distribution produced by the injection probes above a PCB, comparisons between measurements and simulations of the voltage induced by injection probes on a microstrip line are carried out. The case study is a 75 mm long microstrip line designed over a PTFE substrate (ε_r = 2.2, tan δ = 0.01). The substrate thickness is set to 1.5 mm and the line width is equal to 2.8 mm. With these dimensions and material, the characteristic impedance Z_C is equal to 67 Ω and the effective permittivity ε_{eff} is 1.82. The line is terminated by 50 Ω loads at each end. E and H-field injection are done, with the calibrated probes presented in Section III.B. They are placed either at R = 1 or 4 mm above the center of the line. Simulations are performed with the 3D electromagnetic solver FEKO [20]. The injection probes are modeled as elementary electric or magnetic dipoles with the moment extracted during the calibration. They are placed at a distance r above the microstrip line model given by (64), where h_{inj} is the injection height extracted by calibration.

$$r = R + h_{eff} + h_{inj} \quad (64)$$

The comparisons between measurements and simulations of the NF couplings are presented in Fig. 10. Good agreement between measured and simulated voltages is observed up to 3 GHz, regardless of the scanning height, proving the relevance of the probe calibration method and field distribution computation. The small discrepancies are related to errors on probe calibration, line modeling, and parasitic common-mode coupling that can affect E-field injection results.

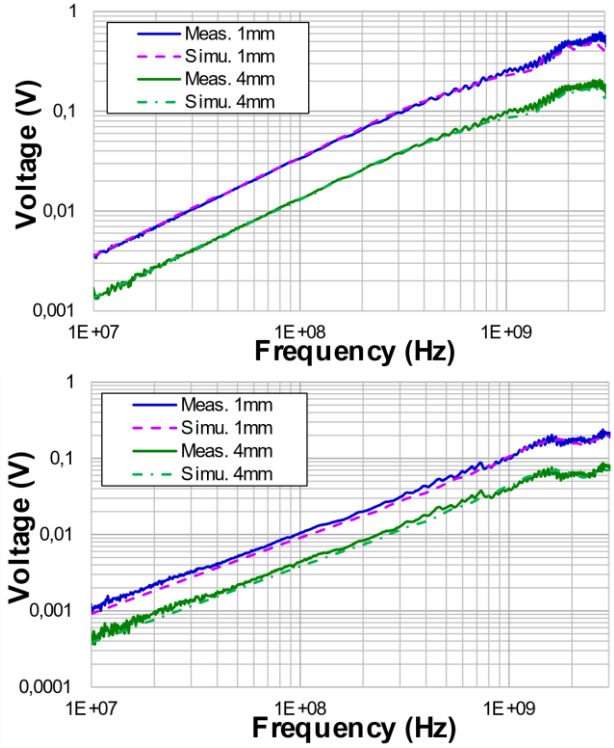

Fig. 10. Comparison between measurement and simulation of the voltage induced on a microstrip line by: the NF H-field probe (top), the NF E-field probe (bottom)

IV. Verification by Simulation of the NF-based FF-coupling Estimator

In order to verify the NF-based FF-coupling estimator proposed in Section II.C, simulations are performed on five models to compare the worst-case voltage induced on a microstrip line illuminated by a plane wave, and its estimation based on NFSI results. All the simulations are made with the 3D electromagnetic software FEKO [20]. The illumination source is either a plane wave with arbitrary angles of incidence and polarization, or an elementary electric or magnetic dipole placed in an arbitrary position above the line under test. To determine the worst-case FF-induced voltage, a first simulation consists in repeating it with a sweep of θ, φ and ψ on their definition range every 15°. The amplitude of the plane wave (E_0 = 100 V/m), the characteristics of the line, and the terminal loads are constant. Then, two parametric NF injection simulations are performed: one with a 1 µA·m elementary electric dipole, the other with a 1 µA·m² elementary magnetic dipole, both placed at 1 mm above the line under test. In these simulations, the position of the probe is swept every 2 mm along the line. At each frequency, the maximum voltage induced on the line terminal is saved as well as the average E or H field produced by the probe along the line under test. Finally, as the average fields are required to scale the induced voltage to the field amplitude applied during plane wave illumination, the two last simulations consist in simulating the near-field produced by either the electric or the magnetic dipoles without the line under test. The impact of the substrate is accounted for according to the approach given in Section III. C.

The case study presented in Section III.D is reused.

Simulations are performed between 10 MHz and 10 GHz. Fig. 11 presents the comparison of the simulations of the worst-case FF coupled voltage with two versions of the NF-based estimators: "NF-to-FF estimator" relies on the exact knowledge of ε_{eff} and is given by (50), while "NF-to-FF estim. simplified" is an approximated version where the exact value of ε_{eff} is assumed to be unknown and set to ε_r.

Four case studies with different loading conditions are considered, and results are shown in Fig 11: perfect matching, two identical resistors, either larger or smaller than Z_C, and two complex loads. When the line terminations are perfectly matched (Fig. 11-a), the FF-coupling estimator provides an exact upper bound of the maximum voltage induced during FF illumination of the line. When the line is not matched, this estimator tends to overestimate the maximum FF-induced voltage observed during resonances (up to +43 % in Fig. 11-b, +120 % in Fig. 11-c, and +52 % in Fig. 11-d), especially when the real part of Γ_2 is negative, as can be expected due to the term $|\Gamma_2|$ in the HF worst case NF-induced voltage (45) and (46). However, the estimator reproduces the fluctuations of the FF-induced voltage according to frequency and, in particular, the maxima due to line resonances. This overestimation can be reduced if the approximated estimator is used (up to +12 % in Fig. 11-b, +67 % in Fig. 11-c and +16 % in Fig. 11-d), except when the line is nearly matched at each termination. In this case, the worst-case FF-induced voltage is slightly underestimated (up to -21 % in Fig. 11-a). These results prove that the FF-coupling estimator is able to provide the worst-case induced voltage on a line illuminated by a plane wave, with a sufficient level of precision for RI risk assessment. They also confirm that it can be obtained irrespective of the loading conditions, line geometry, and materials, and the knowledge of ε_{eff} is not absolutely required.

V. Comparison between NFSI and TEM Cell Results

In this part, the NF-based FF-coupling estimator is evaluated by comparing between NFSI and RI measurement results. Due to the small size of the microstrip line, the large distance to the illuminating antenna and the presence of connection cables which may act as parasitic antenna, the RI test in ALSE is not precise and repeatable enough to validate the proposed estimator. A more convenient approach, particularly adapted for the RI test at the PCB and IC levels, is the TEM/GTEM cell. Although the polarization of the TEM wave within the cell is fixed, the method is far more repeatable than tests in ALSE. The field amplitude within the TEM cell is known with good precision and can reach several hundred V/m, with excitation of only a few watts. The line under test can be oriented according to four directions as described in Fig. 12: either in parallel with the septum (0° and 180°) or perpendicular (90°, 270°). Despite the reduced number of angles of arrival of the plane wave, 0 and 180° orientations are worst-case orientations in LF and they may be sufficient to evaluate the robustness of the estimator.

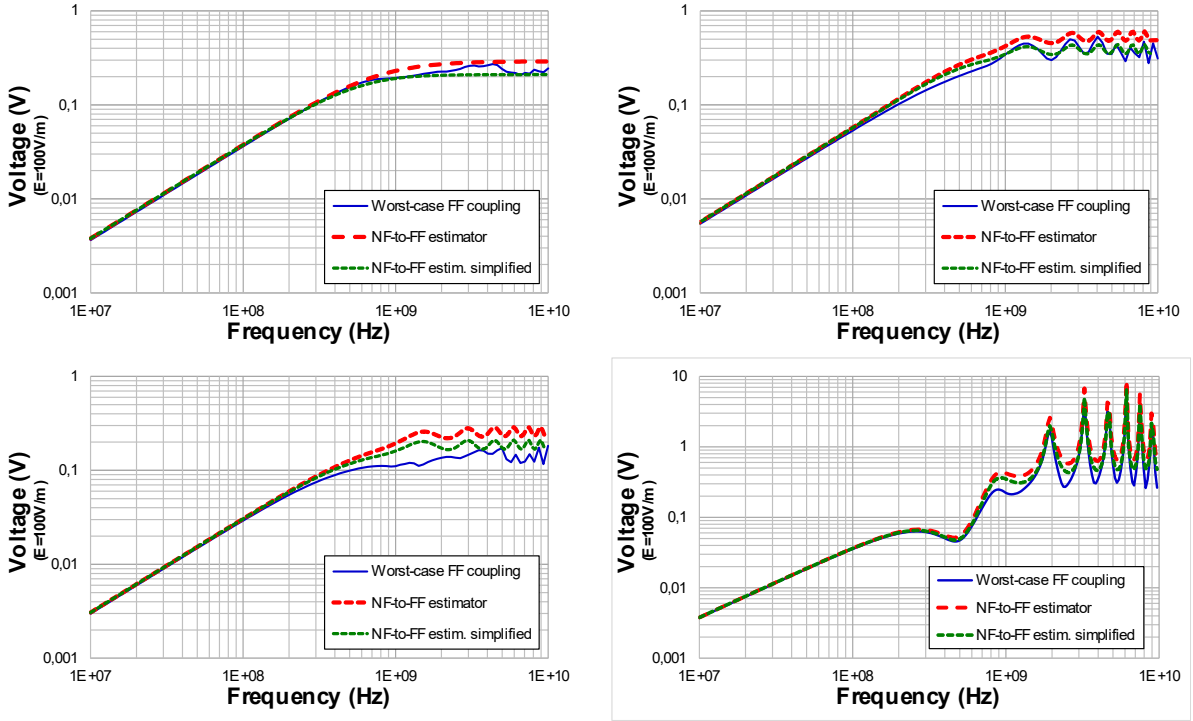

Fig. 11. Comparison between simulated worst-case FF coupling and NF-to-FF coupling estimators: (a) $Z_{L1} = Z_{L2} = Z_C$ (top left), (b) $Z_{L1} = Z_{L2} = 2Z_C$ (top right), (c) $Z_{L1} = Z_{L2} = 0.5Z_C$ (bottom left), (d) $Z_{L1} = Z_C$//10 pF + 10 nH, $Z_{L2} = Z_C$ + 10 nH (bottom right)

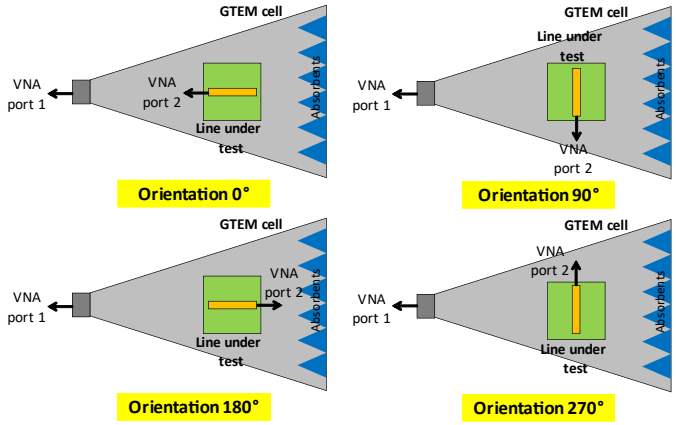

Fig. 12. Orientation of the line under test in the GTEM cell

The line under test has the same characteristics as the one presented in Section III.D. It is terminated either by 50 Ω loads on both sides, or by a 150 Ω-to-50 Ω transformer on one side and a 10 pF capacitor on the other. RI tests are carried out with a GTEM cell, model Schaffner GTEM250. NFSI tests are performed with the probes calibrated in Section III, placed either at 1 or 4 mm above the line under test. In both cases, a VNA is used to measure the transmission coefficient S_{12} between the GTEM cell or the injection probe and the line under test. Before NFSI tests, the S-parameters of the line under test are measured and compared with and without the presence of the injection probe, in order to verify that the probe does not affect the characteristics of the line under test. GTEM results are scaled according to (65) to determine the induced voltage V_{GTEM} for an E-field amplitude equal to 100 V/m, where h_{GTEM} is the distance between the line and the GTEM septum. NFSI results are used to evaluate the worst-case induced voltage in GTEM cells according to the estimator defined in (52) and the average E and H field produced by the injection probes from the probe calibration results. Measurements are performed between 10 MHz and 3 GHz, as the injection probes are properly calibrated up to this frequency.

$$V_{GTEM} = S_{12} h_{GTEM} E \tag{65}$$

Fig. 13 compares the GTEM cell results for the four orientations with the NF-based FF-coupling estimator obtained at both scanning heights, when the line is terminated by 50 Ω resistors on each side. Up to 900 MHz, there is excellent agreement between the worst-case induced voltage in GTEM, obtained for the 0° orientation, and its estimation. In this frequency range, the line is electrically small. Above 900 MHz, the line becomes electrically long. The induced voltage follows a complex relationship with the frequency, incidence and polarization angles, as highlighted in Section II.B. This results in the presence of periodic minima and maxima whose frequencies depend on the line orientation. The NF-based estimation provides a correct upper bound of the worst-case GTEM voltage up to 3 GHz. Estimations based on scanning results at two different heights are very similar, proving that the estimation does not depend on the scanning height, as long as the injection height has been correctly extracted during the calibration.

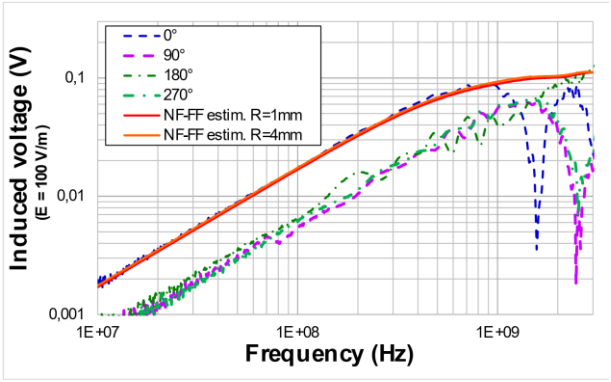

Fig. 13. Comparison between measurements of the induced voltage on a microstrip line terminated by 50-Ω loads for 4 orientations in GTEM cells, and estimation based on NFSI done at two different scanning heights

In Fig. 14, the terminations are replaced by 150 Ω and 10 pF terminations. The small difference between the NF-based estimations at both scanning heights below 30 MHz is related to the lower level of coupling between the injection probes and the line under test in LF. The evolution vs. frequency of the voltage induced in GTEM is more complex, because of the non-constant termination impedance. Numerous peaks arise above 300 MHz, depending on the line orientation. Once again, NF-based estimation provides an upper bound of the worst-case GTEM voltage up to 3 GHz. All the peaks observed in GTEM results also appear on the NF-based estimation, proving that this estimator can detect line resonance frequencies, regardless of the orientation of the incoming radiated disturbance. Contrary to the previous case, the estimator tends to overestimate the GTEM-induced voltage (from +3 % to + 90 % at the resonant frequencies) because the NF-based estimator cannot completely capture the effect of the termination load. However, this estimation can be precise enough to anticipate RI risks at the PCB level during a preliminary NFSI campaign.

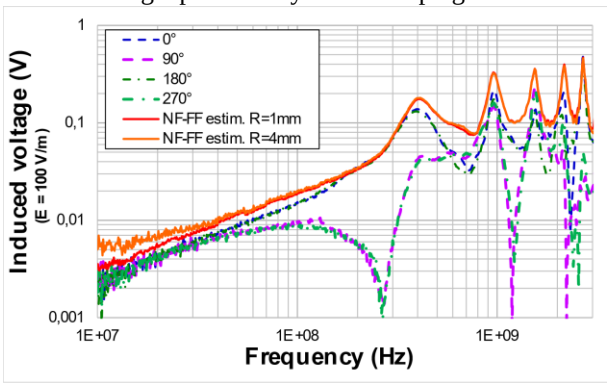

Fig. 14. Comparison between measurements of the induced voltage on a microstrip line terminated by 150-Ω and 10 pF loads for 4 orientations in GTEM cells, and estimation based on NFSI done at two different scanning heights

VI. Conclusion

NFSI is a valuable method for the analysis of root-cause of radiated susceptibility at the circuit and board level. However, a method to extrapolate radiated immunity result from NFSI is still lacking. This paper has addressed this issue. The equivalence between near-field and far-field coupling has been discussed in the case of a typical PCB interconnect: a microstrip

line, terminated by linear loads, and an estimator of the induced voltage at line terminal based only on NFSI results has been derived. Even though this estimator cannot precisely predict the actual induced voltage for a given plane-wave, it is able to provide the worst-case induced voltage regardless of the angles of arrival and polarization of the incoming wave. In addition to the root-cause detection of failures, this estimator provides NFSI with a method to assess radiated immunity at the PCB level. This estimator has been validated by measurement and simulation at least up to 3 GHz. One important requirement for this method is the calibration of the injection probe, to determine the field produced along PCB interconnects. The paper also presented and validated a calibration method, since no standard calibration procedure for NF injection probes was available. With the proposed calibration method, the field produced by the injection probe in the near-field region can be determined through a simple model, regardless of the characteristics of the board under test.

The proposed method is currently valid only for straight microstrip lines. In the case of a bent microstrip line, several H-field components may couple on different parts of the line. The mathematical formulations presented in this paper need to be adjusted for this more complex geometry. Further studies are required to validate the proposed methodology not only on a bent microstrip line, but also on more complex line structures (e.g., coplanar waveguide, edge-coupled microstrip). One limitation of the proposed approach is that passive linear loads terminate the tested PCB interconnect. Moreover, it gives the induced voltage for a given field amplitude but, in practical radiated susceptibility tests, the field amplitude which triggers a failure is looked for. Both issues will be addressed in the second part of this paper.

REFERENCES

[1] A. Boyer, E. Sicard, S. Bendhia, “Characterization of the Electromagnetic Susceptibility of Integrated Circuits using a Near Field Scan”, *Elec. Letters*, vol. 43, No 1, pp. 15-16, 4th Jan. 2007, 10.1049/el:20073130.

[2] IEC TS 62132-9, Integrated circuits – Measurement of electromagnetic immunity – Part 9: Measurement of radiated immunity – Surface scan method, International Electrotechnical Commission, 2014.

[3] N. Lacrampe, S. Serpaud, A. Boyer, S. Tran, "Radiated Susceptibility Investigation of Electronic Board from Near Field Scan Method", *in Proc. EMC Compo 2017*, Saint Petersburg, Russia, Jul. 2017, pp. 125-130.

[4] A. Alaeldine, T. Ordas, R. Perdriau, P. Maurine, M. Ramdani, L. Torres, M. Drissi, "Assessment of the Immunity of Unshielded Multicore Integrated Circuits to Near Field Injection", *in Proc. Int. Zurich Symp. on EMC*, Zurich, Switzerland, Jan. 2009, pp. 361-364.

[5] A. Boyer, S. Bendhia, E. Sicard, "Modelling of a Mixed-Signal Processor Susceptibility to Near-Field Aggression", *in Proc. 2007 IEEE Int. Symp. on EMC*, Hawaii, USA, Jul. 2007.

[6] T. Dubois, J. J. Laurin, J. Raoult, S. Jarrix, "Effect of Low and High-Power Continuous Wave Electromagnetic Interference on a Microwave Oscillator System: From VCO to PLL to QPSK Receiver", *IEEE Trans. on EMC*, vol. 56, no. 2, pp. 286-293, Apr. 2014, 10.1109/TEMC.2013.2280670.

[7] O. Kröning, M. Krause, M. Leone, “Near Field-Immunity Scan on Printed Circuit Board Level”, *in Proc. 2010 IEEE 14th Workshop on Signal Propagation on Interconnects (SPI)*, May 2010, pp. 101-102.

[8] K. Wang, D. Pornmerenke, J. M. Zhang, R. Chundru , “The PCB level ESD immunity study by using 3 Dimension ESD Scan System”, *in Proc. 2004 Int. Symp. on EMC*, Aug. 2004, pp. 343-348.

[9] D. Pommerenke, G. Muchaidze, J. Koo, Q. Cai, J. Min, “Application and Limits of IC and PCB scanning methods for immunity analysis”, in Proc. 18th Int. Zurich Symposium on EMC, Munich, Germany, Sept. 2007, pp. 83-86.

[10] M. Leone, H. L. Singer, “On the Coupling of an External Electromagnetic Field to a Printed Circuit Board Trace”, *IEEE Trans. on EMC*, vol. 41, no. 4, pp. 418-424, Nov. 1999, 10.1109/15.809842.

[11] J. Xiao, D. Pommerenke, J Min, H. Wei, G. Muchaidze, “Local probe injection compared to direct ESD injection”, *in Proc. EMC Compo 2009*, Toulouse, France, Nov. 2009.

[12] A. Durier, S. Ben Dhia, T. Dubois, “Comparison of Voltages Induced in an Electronic Equipment during Far Field and Near Field Normative Radiated Immunity Tests”, *in Proc. of 2019 Int. Symp. On EMC - EMC Europe 2019*, Barcelona, Spain, Sep. 2019.

[13] J. J. Wang, “An Examination of the Theory and Practices of Planar Near-Field Measurement”, *IEEE. Trans on Antennas and Propagation*, vol. 36, no. 6, June 1988, pp. 746-753.

[14] A. Boyer, “Improving Spatial Resolution of Immunity Maps by Post-Processing”, *in Proc. of 2016 Asia-Pacific Int. Symp. on EMC (APEMC)*, Shenzhen, China, May 2016, pp. 56-59.

[15] A. Boyer, “A Rigorous Method to extrapolate Radiated Susceptibility from Near-Field Scan Immunity”, *in Proc. 2019 Int. Symp. on EMC - EMC Europe 2019*, Barcelona, Spain, Sep. 2019.

[16] A. K. Agrawal, H. J. Price, S. H. Gurbaxani, “Transient response of multiconductor transmission lines excited by a nonuniform electromagnetic field,” *IEEE Trans. on EMC*, vol. 22, no. 2, pp. 119–129, May 1980.

[17] F. Rachidi, “Formulation of the field-to-transmission line coupling equations in terms of magnetic excitation field,” IEEE Trans. on EMC, vol. 35, no. 3, pp. 404–407, Aug. 1993.

[18] C. D. Taylor, R. S. Satterwhite, W. J. Harrison, "The response of terminated two-wire transmission line excited by a non uniform electromagnetic field", *IEEE Trans. on Antennas and Propagation*, vol. AP-13, pp. 987-989, 1965.

[19] F. M. Tesche, M. Ianoz, T. Karlsson, *EMC Analysis Methods and Computational Models*, Wiley, 1996, 978-0-471-15573-7.

[20] Altair FEKO, Electromagnetic Simulation Software, more information on www. altairengineering.fr/feko.

[21] J. Raoult, P. Payet, R. Omarouayache, L. Chusseau, “Electromagnetic Coupling Circuit Model of a Magnetic Near-Field Probe to a Microstrip Line”, *in Proc. 10th International Workshop on the Electromagnetic Compatibility of Integrated Circuits (EMC Compo 2015)*, Edinburgh, UK, Nov. 2015.

[22] M. Krause, M. Leone, “Calibrated Time-Domain Near Field-Immunity Test on Printed-Circuit Board Level”, *in Proc. 2013 Int. Symp. on EMC (EMC Europe 2013)*, Brugge, Belgium, Sept. 2013.

[23] A. Boyer, "Méthode de prédiction de la compatibilité électromagnétique des systèmes en boîtier", Ph.D. dissertation, INSA Toulouse, Univ. of Toulouse, Toulouse, France, 2007.

[24] A. Boyer, N. Nolhier, F. Caignet, S. Ben Dhia, “Closed-Form Expressions of Electric and Magnetic Near-Fields for the Calibration of Near-Field Probes”, *IEEE Trans. on Instr. and Meas.*, early access, Nov. 9th 2021, pp. 1-14, 10.1109/TIM.2021.3126376

[25] P. Silvester, “TEM wave properties of microstrip transmission lines”, *in Proc. Inst. Elec. Eng.*, vol. 115, no. l, pp.43–4S, Jan. 1968.

A. Boyer obtained a Masters degree in electrical engineering in 2004 and a PhD in Electronics from the French National Institute of Applied Sciences (INSA) in Toulouse, France, in 2007. He is currently an Associate Professor in the Department of Electrical and Computer Engineering at INSA, Toulouse. He carries out research at the Laboratory of Analysis and Architecture of Systems (LAAS-CNRS), as part of the ‘Energy and Embedded Systems’ research group. His current research interests include EMC measurements, IC EMC and reliability modeling, and computer aided design (CAD) tool development for EMC (IC-EMC freeware).

N. Nolhier received a doctorate in electronics from the French National Institute of Applied Sciences (INSA), Toulouse, in 1992. He is Professor at the University Paul Sabatier, Toulouse, and works at the Laboratory of Analysis and Architecture of Systems (LAAS-CNRS). First motivated by the control and modeling of rapid heat treatment, his interests shifted to the design and simulation of Power Devices. In 1996, he initiated the study of ESD protections using 2D electrothermal simulations at LAAS and studied TLP experiments. He has supervised more than 15 PhDs in ESD protection strategy (device and system level). Since 2016, he has focused on the reliability of space nanosystems. In 2019, he became director of the Toulouse University Space Center (CSUT).

F. Caignet received an MS degree in electrical engineering from the University of Toulouse, Toulouse, France, in 1995, and a PhD degree from the French National Institute of Applied Sciences (INSA), Toulouse, in 1999. From 1995 to 2000, he worked on signal integrity and EMC at the chip level at INSA. In 2001, he joined the Laboratory of Analysis and Architecture of Systems (LAAS), Toulouse, to work on the integration of optical links and devices into silicon chips, tackling challenges like propagation time on high complex architectures, EMC aspects, and cost. In 2006, he joined the electrostatic discharge (ESD) team of LAAS to work on ESD at a system level. His current research interests include developing measurement and simulation methodology to predict ESD impact at the IC level.

S. Ben Dhia obtained her Masters degree in electrical engineering in 1995, and a PhD in Electronic Design from the French National Institute of Applied Sciences (INSA), Toulouse, France, in 1998. Full professor at INSA-Toulouse (French engineering institute), Department of Electrical and Computer Engineering, she teaches digital electronics, IC testability and reliability, and analog and RF CMOS design. CEO of INSA Euro-Méditerranée, Fès, Morocco (2014-2017), she was responsible for the overall leadership and management of this new engineering institute. Her research interests at LAAS – CNRS Toulouse include signal integrity in nano-scale CMOS ICs, electromagnetic compatibility and reliability of ICs. She has authored or co-authored 3 books, more than 120 publications in peer-reviewed journals and conference proceedings, and supervised 14 PhD theses and 9 MSc theses.